Pinning in a Contact and Noncontact Manner: Direct Observation of a Three-Phase Contact Line Using Graphene Liquid Cells

Hirokawa, Sota
Department of Aeronautics and Astronautics, Kyushu University

Teshima, Hideaki
Department of Aeronautics and Astronautics, Kyushu University

Solis-Fernandez, Pablo
Global Innovation Center, Kyushu University

Ago, Hiroki
Global Innovation Center, Kyushu University

他

https://hdl.handle.net/2324/4793219

出版情報：Langmuir. 37 (42), pp.12271-12277, 2021-10-26. American Chemical Society
バージョン：
権利関係：

Pinning in contact and non-contact manner: Direct observation of three-phase contact line using graphene liquid cells

Sota Hirokawa[1, 2], *Hideaki Teshima*[1], *Pablo Solís-Fernández*[3], *Hiroki Ago*[3], *Qin-Yi Li*[1,2],

*Koji Takahashi** [1,2]

[1] Department of Aeronautics and Astronautics, Kyushu University, 744 Motooka, Nishi-ku, Fukuoka 819-0395, Japan

[2] International Institute for Carbon-Neutral Energy Research (WPI-I2CNER), Kyushu University, 744 Motooka, Nishi-ku, Fukuoka 819-0395, Japan

[3] Global Innovation Center, Kyushu University, 6-1 Kasuga-koen, Kasuga-city, Fukuoka 816-8580, Japan

* email: takahashi@aero.kyushu-u.ac.jp phone: +81-92-802-3015

Abstract

Pinning of a three-phase contact line at the nanoscale cannot be explained by conventional macro-scale theories, and thus requires an experimental insight to understand this phenomenon. We performed in-situ TEM observation of the three-phase contact lines of bubbles inside graphene liquid cells to experimentally investigate the causes of nanoscale pinning. In our observations, the three-phase contact line was not affected by the 0.6 nm-thick inhomogeneity of the graphene surface, but thicker metal nanoparticles with diameters of 2–10 nm and nano-flakes caused pinning of the gas-liquid interface. Notably, we found that flake-like objects can cause pinning that prevents the bubble overcome the flake object in a non-contact state, with a 2-nm-thick liquid film between them and the bubble. This phenomenon can be explained by the repulsive force obtained using the Derjaguin, Landau, Verwey, and Overbeek theory. We also observed the flake temporally prevented the gas-liquid interface moving away from the flake. We discussed the physical mechanism of the attractive force–like phenomenon by considering the nanoconfinement effect of liquid sandwiched by two graphene sheets and the hydration layer formed near the solid surface.

Introduction

Pinning, which interferes with the dynamics of the solid-liquid-gas three-phase contact line, governs the motion, growth, collapse and even the shape of droplets and bubbles. Pinning affects many applications, including microfluidics[1], self-cleaning materials[2], and phase-change heat transfer[3], and becomes more pronounced at the sub-micron scale. For example, surface nanobubbles are expected to self-collapse within a few milliseconds due to the Laplace pressure of several MPa caused by their radius of curvature of several hundred nanometers. However, in reality, the strong pinning at the three-phase contact line makes the bubbles very flat and enlarges the radius of curvature, enabling the bubbles to have a long lifetime of several hours to several days[4,5]. In addition, interfacial nanobubbles are resistant to disturbances such as ultrasonic waves and heating to near boiling point; which is also attributable to pinning, according to both experimental and theoretical studies[6–9]. In the case of nanodroplets, deviations from the macroscopic contact angle with decreasing size are also observed, which cannot be explained by line tension, suggesting the involvement of pinning[10]. These experimental findings suggest that pinning plays a more dominant role in nanoscale fluid behavior than surface tension does.

According to conventional theories confirmed by macroscopic experiments, pinning is caused by chemical and mechanical inhomogeneities on the solid surface, just below the three-phase contact line[11,12]. However, the origin of pinning at the nanoscale is still unclear. As mentioned above, it has been reported that the three-phase contact line of interfacial nanobubbles is strongly pinned[13], but most of the interfacial nanobubbles that have been studied were generated on graphite substrates, which are atomically smooth with no surface inhomogeneity. Therefore, the macroscopic factors considered in the classical theories cannot explain the nanoscale pinning phenomenon. One possible origin of nanoscale pinning is the friction between solid-liquid interfaces caused by local potential waveforms brought about by discrete solid surface atoms[14]; however, molecular dynamics (MD) simulations of droplets using Lennard Jones (LJ) fluids have demonstrated that Young's equation holds at the nanoscale for the surfaces[15]. In addition, recent experimental and simulation studies showed that, on a solid surface impregnated with a liquid, structures on the scale of several nanometers, such as adsorbed gas-molecule layers and hydration structures, are formed[15–18]. Because such structures (which are overlooked in conventional macroscopic studies) locally change the properties of the fluids[16,19,20], it is important to take them into consideration to correctly understand the fundamental pinning mechanism.

In this study, we conducted nanoscale in situ observations in the vicinity of the three-phase contact lines using transmission electron microscopy (TEM) to investigate the causes of pinning. While sufficiently small chemical and mechanical heterogeneities did not affect the three-phase contact lines, relatively large particles and flake-like contamination pinned them. While pinning was caused by particles in contact with the three-phase contact line, it was observed that pinning also occurs when a thin liquid film is maintained between the flakes and the three-phase contact line (i.e., a "non-contact" scenario). This physical mechanism was qualitatively explained by discussing the forces between the bubble and the flake using the Derjaguin, Landau, Verwey, and Overbeek (DLVO) theory, and considering the effect of the hydration structure.

Experimental

Sample fabrication

To visualize bubbles and water using TEM, we encapsulated them between the two bilayer graphene sheets; it is known as graphene liquid cells (GLCs)[21]. A schematic image of TEM observation and cross-section of the GLC is shown in the supporting information. Our bilayer graphene was synthesized on a Cu/Ni film on a sapphire substrate by chemical vapor deposition (CVD). Detailed methods for our graphene synthesis are given in reference[22]. A TEM grid (R1.2/1.3 Au 200 mesh, Quantifoil Micro Tools GmbH, Germany) was placed directly onto the graphene and Cu/Ni; the Cu/Ni-graphene grid system was then immersed in 0.2 M ammonium persulfate solution to etch the Cu/Ni film. The resulting graphene-TEM grid was moved from the etchant to pure water and washed three times, changing the water each time. After drying in a clean room environment for 2 hours, approximately 0.5 μL air-saturated pure water was dropped on the graphene side of the TEM grid. Another graphene-TEM grid was then gently placed on top of the water bead to create a sandwich structure with water trapped between the two graphene sheets. The droplet was broken up into many small liquid cells when the two graphene sheets came into contact. Because upper and lower graphene sheets were firmly stacked via the van der Waals force, and they are gas-impermeable[23–25], the encapsulated water was effectively protected from the ultrahigh vacuum environment of the TEM column. The atomic thinness of graphene allows for the observation of liquid samples with highest spatial resolution. In addition to GLCs, a dry graphene-TEM grid sample was prepared to measure the graphene height profiles and observe any features which might induce pinning.

Observation method

We used the frequency modulation (FM) mode of an SPM-8100FM atomic force microscope (AFM) made by Shimadzu Corp., Japan for observation of the graphene surface. An AC200TN cantilever (OLYMPUS Corp., Japan) with a tip radius of 7 nm was used. The height data were captured with a resolution of 256 × 256 pixels and scan rate of 0.8 Hz. Because bilayer graphene is atomically thin, its surface profile on any substrate will inevitably be influenced by the surface condition of the substrate. Thus, we aimed to analyze the part of our graphene-TEM grid where the graphene was suspended over the holes in the support membrane.

The Graphene-TEM grid sample was also imaged in a transmission electron microscope (JEM-2100Plus, JEOL Ltd., Japan), operating at an accelerating voltage of 200 keV. Comparing the AFM images and the TEM images provided us with more detailed information about the graphene surface. We also used a JEM ARM200CF (JEOL Ltd., Japan) at 60 keV for the in-situ imaging of the GLCs. This TEM has a cold field-emission electron gun, whose brightness reaches ~1 × 10^9 A/cm^2, thus enabling us to obtain higher spatial resolution images than those obtained with the LaB_6 electron gun used in the JEM-2100Plus.

Results and Discussion

Graphene surface inhomogeneity and its influence

Although graphene is widely regarded as an atomically-smooth two-dimensional material, its real surface contains inhomogeneities due to the inevitable contamination. In the TEM image of the graphene transferred onto the TEM grid (Figure 1(a)), the contamination appears as camouflage-like pattern with a slightly darker color than the color of the clean area. Considering that TEM electron beam penetration is affected by the atomic number of the material and that both clean and contaminated areas have similar gray values, these impurities were assumed to be carbon atoms that did not crystallize during the CVD process, or hydrocarbon contamination from liquids or air that absorbed on the surface during the transfer. Similar camouflage patterns on graphene have also been observed in previous studies and treated as contamination[26–28]. Figure 1(b) shows the height image of the suspended graphene surface obtained by FM mode AFM. Figure 1(c) shows the height profiles including the contamination peaks (upper left and right). The orange line profile in Figure 1(c) shows that the contamination creates a terrace structure with a height of about 0.6 nm. Also, the blue line profile changes by around 0.5 nm, which is comparable to the size of single carbon atom (0.33 nm), over a long distance of 1 μm. In summary, the graphene used in this experiment had an arithmetic mean roughness (Sa) of about 0.2 nm, and its maximum peak height and minimum pit depth were 1 nm.

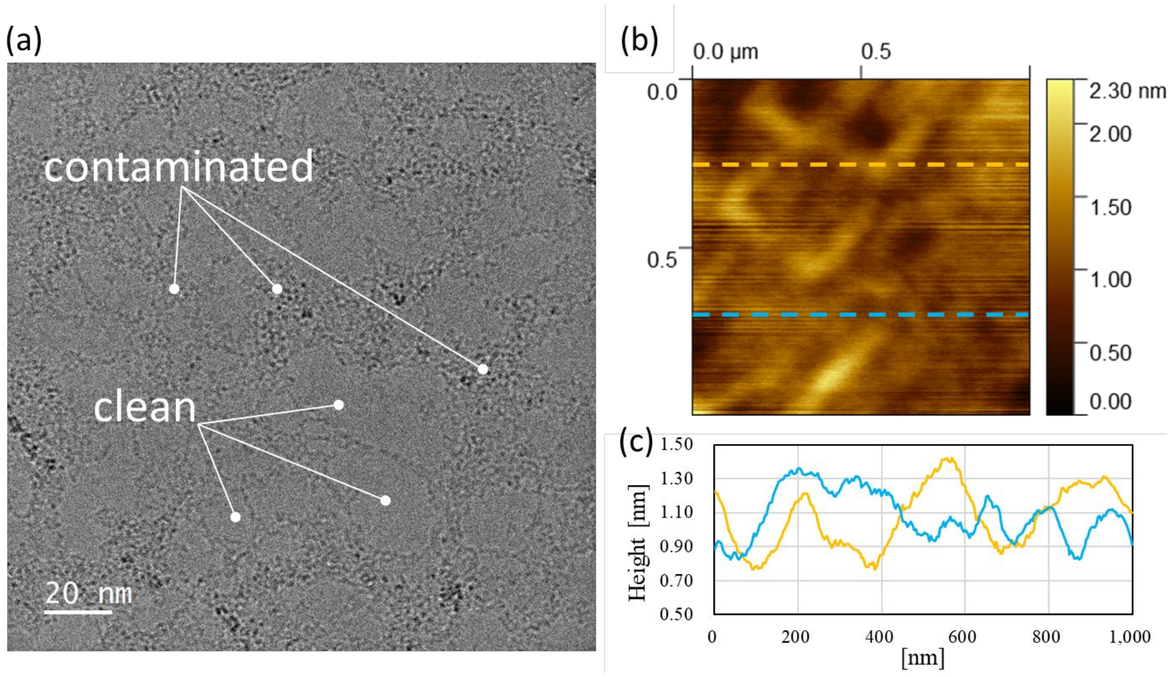

Figure 1 (a) TEM image of the suspended graphene transferred onto a TEM grid. (b) The height image of the suspended graphene measured with FM-AFM. (c) The

height profiles measured along the orange and blue lines in (b). Both (a) and (b) were taken from the same sample, but they were not in the exact same area.

TEM observations of the sample prepared by sandwiching water droplet between these graphene-TEM grids showed that there were many GLCs in a single sample, and more than half of the GLCs contained bubbles, as shown in Figure 2(a). The GLCs ranged from 100 nm to 1 μm in diameter, and the bubbles occupied about 20%–85% of their GLC area.

The main point of interest is the shape of the bubble. The contour line of the bubble shown in Figure 2(a), i.e., the three-phase contact line, is not affected by the inhomogeneity of the graphene surface and maintains a thermodynamically stable circular shape. We identified that surface inhomogeneity can be neglected due to the sufficiently small size of the terrace structure created by contamination. We previously estimated that the thickness of the liquid cell prepared by the same procedure as this study was about 10 nm, based on the Brownian motion of the nanoparticles inside the liquid cell[29]. We also mentioned that the bubbles were in contact with both the upper and lower graphene layers and existed in cylindrical shapes. Assuming that the characteristic length of the GLC surface is 0.6 nm from the height of the terrace structure shown in Figure. 1(c), the bubble height is approximately 16 times larger than that of the surface structure. In addition, the effect of chemical heterogeneity between the graphene surface and the contamination was negligible. This may be because the airborne contamination is mainly composed of carbon atoms, as is the graphene.

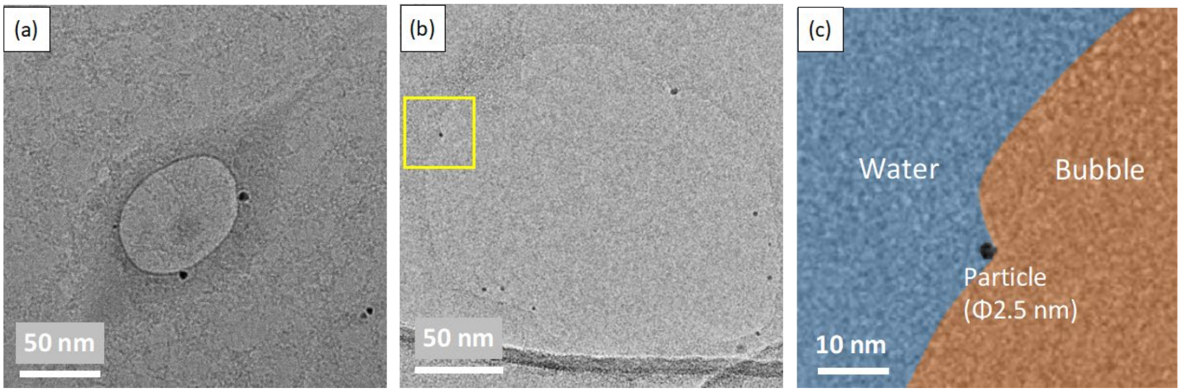

Figure 2 (a) TEM image of GLC and the encapsulated bubble. (b) TEM image of the bubble whose interface was pinned by the nanoparticle and (c) The enlarged view of the yellow box area in (b). Water is colored blue, and the bubble is colored orange. The original TEM image of (c) is shown in Figure S2 in the supporting information.

Pinning in contact manner

In contrast to the carbon-based surface inhomogeneities, nanoparticles with diameters of 2–10 nm, assumed to be residues from the Cu/Ni film, have a pinning effect when in contact with the gas-liquid interface, as shown in Figure 2(b, c). The contour of the deformed liquid-gas interface was almost logarithmic as predicted in previous study[30] (the detail is shown in supporting information). The nanoparticles that caused pinning were sandwiched between the top and bottom graphene sheets, and were therefore completely immobile. When the nanoparticles are not fixed, Brownian motion is usually expected[29]. Since the Figure 2(b, c) show the contact point of gas-liquid interface on the nanoparticle, it seems that the contact angle of the nanoparticle can be determined by measuring the angle between the tangential line of the particle and the gas-liquid interface (the TEM image of the contact angle on the nanoparticle is shown as Figure S4 in the supporting information). However, it is very difficult to accurately evaluate the contact angle on such nanoparticles from this TEM image, because of the three-dimensional nature of the nanoparticles, and the insufficient resolution of the gas-liquid interface in the image. The gas-liquid interface will appear as a hazy region, even at sufficiently high resolutions. This is because there is no well-defined gas-liquid interface as described in thermodynamics (Gibbs' dividing plane) at this scale[31], instead there is a subnanometer-thick region in which the molecular density changes continuously, as is often observed in MD simulations[32]. Therefore, it would be difficult to apply the thermodynamic definition of contact angle at this scale, which considers the gas-liquid interface to be a definite surface. Also, we would like to clarify that the size of these nanoparticles (~2 nm) is not the threshold for pinning caused by structural inhomogeneity, because its strength is determined not only by structural heterogeneity but also by chemical heterogeneity, which may be significantly large between the metal particle and the graphene.

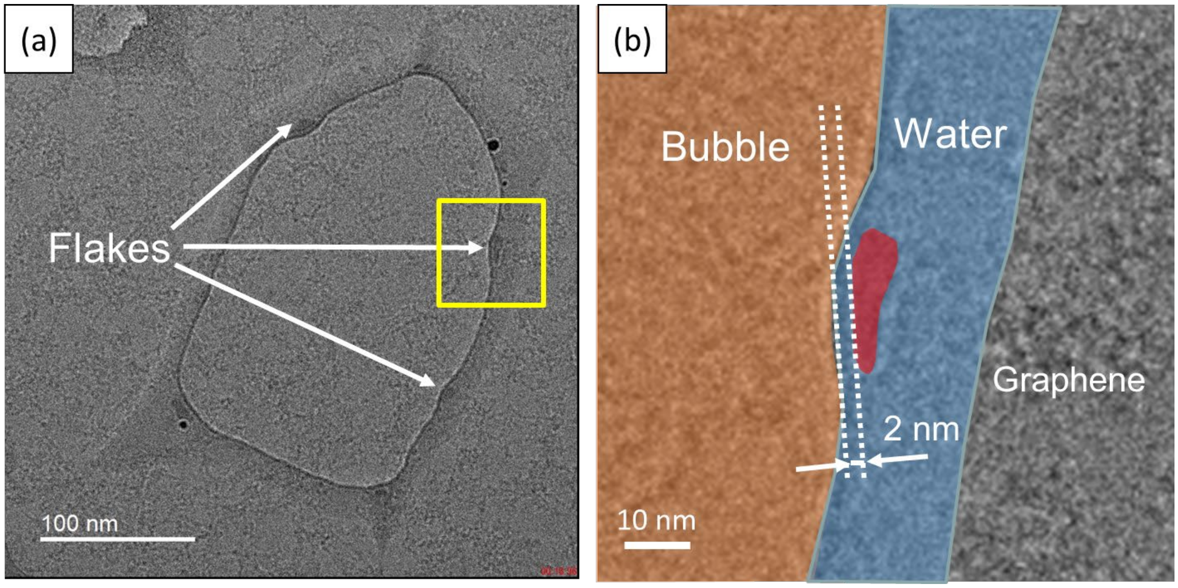

Figure 3 (a) TEM image of a bubble pinned by flake-like objects. (b) The enlarged view of the yellow box region in (a). The flake is colored in red. The original TEM image of (b) is shown in the supporting information.

Non-contact pinning

Further observation revealed that the gas-liquid interface was deformed by flake-like materials that appear as areas which are darker than the water but lighter than the particles, as shown in Figure 3(a). The flakes were observed only when an acceleration voltage of 60 keV was used in the ARM200CF TEM equipped with a field-emission electron gun. The field-emission electron gun provides a more stable electron beam, with a high current density; and, using a low-energy electron beam increases the collision rate between the flake atoms and the electrons, which made their observation possible. This suggests that the flakes were very thin and made of light atoms, such as carbon, which are easily penetrated by electron beams. Interestingly, there was no direct contact between the flakes and the gas-liquid interface, instead they were separated by a 2 nm thin film of water, as depicted in Figure 3(b). The presence of a thin water film between gas-liquid interface and the flake is clearly shown in Figure S5 in the supporting information.

Figures 3 clearly showed that the flakes pinned the three-phase contact line without contact; however, it has been widely accepted that the pinning force is generated when the three-phase contact line touches surface roughness or chemical heterogeneity. Therefore, our observations cannot be explained by the conventional theory which assumes that contact between the gas-liquid interface and the solid surface is necessary for pinning. To reveal the principle of the non-contact pinning by the flakes, we consider the DLVO theory to discuss the balance between the van der Waals force and the electric double layer force between the bubble and the flake.

At first, the bubble interface and the flake are treated as two different parallel plates. The van der Waals force per unit area, Π_{vdW}, between two parallel plates separated by distance h is calculated as follows:

$$\Pi_{vdw} = -\frac{A}{6\pi h^3} \tag{1}$$

where A is the Hamaker constant, which depends on the objects' properties. In the systems under consideration, there were three different objects, thus the Hamaker constant is expressed as eq. (2)[33]:

$$A = \frac{3}{4}k_B T\left(\frac{\epsilon_1 - \epsilon_3}{\epsilon_1 + \epsilon_3}\right)\left(\frac{\epsilon_2 - \epsilon_3}{\epsilon_2 + \epsilon_3}\right) + \frac{3h_p\nu_e}{8\sqrt{2}}\frac{(n_1^2 - n_3^2)(n_2^2 - n_3^2)}{(n_1^2 + n_3^2)^{1/2}(n_2^2 + n_3^2)^{1/2}\{(n_1^2 + n_3^2)^{1/2} + (n_2^2 + n_3^2)^{1/2}\}} \tag{2}$$

Where k_B is the Boltzmann constant, T is temperature, h_p is the Planck constant, ν_e

is the main electronic absorption frequency in the UV range (typically around 3 × 10^{15} s^{-1}), ϵ is the relative dielectric permittivity, and n is the refractive index. The subscript numbers indicate bubble ($_1$), flake ($_2$), and water ($_3$). The relative dielectric permittivities were assumed to be $\epsilon_1 = 1$, $\epsilon_2 = 2.25$, $\epsilon_3 = 80$, and the refractive indices were $n_1 = 1$, $n_2 = 1.5$, $n_3 = 1.3$[33]. Given the above, at $T = 298$ K, the Hamaker constant took negative value of $A = -2.0 \times 10^{-20}$ J. Substituting into eq. (1), the van der Waals force acting between the bubble and the flake becomes repulsive, $\Pi_{vdW} = 1.35 \times 10^5$ N/m^2.

Next, we consider the electric double layer force. When a solid or a bubble is covered with an electrolyte solution, the electric double layer is formed on the surface through the adsorption and bonding of ions to the surface and the ionization or detachment of surface groups. The electric double layer force, $\mathit{\Pi}_{EDL}$, between two different materials is expressed as in eqs. (3) and (4)[34].

$$\mathit{\Pi}_{EDL} = \frac{2\epsilon_0\epsilon[(e^{+\kappa h} + e^{-\kappa h})\psi_1\psi_2 - (\psi_1^2 + \psi_2^2)]}{(e^{+\kappa h} - e^{-\kappa h})^2} \qquad (3)$$

$$\text{where } \frac{1}{\kappa} = \left\{\frac{\epsilon_3 \epsilon_0 k_B T}{e^2 \Sigma \rho_i z_i^2}\right\}^{1/2} \tag{4}$$

Here, $1/\kappa$ is the Debye length, ψ is the surface potential, ϵ_0 is the permittivity of a vacuum, ρ_i is the number density of ion i, and z_i is its valence. For pure water at room temperature ($T = 298$ K), κ is:

$$\kappa = 3.288\sqrt{I}, \ [\mathrm{nm}^{-1}] \tag{5}$$

I is the ionic strength of pure water, $I_{pure\,water} = 2.5 \times 10^{-6}$ M. Since the surface potential ψ is often approximated by the value of the ζ-potential, we assume that the surface potentials of bubbles and flakes in pure water are $\psi_1 = -20.10$ and $\psi_2 = -45$ mV, respectively[35,36]. Applying these values to eq. (3), the electrostatic force between the bubble and flake in pure water is an attractive force for $h < 3.5$ nm, and $\Pi_{EDL} = 18.5$ N/m^2 for $h = 2$ nm. This value is four orders of magnitude smaller than the van der Waals force $\Pi_{vdW} = 1.35 \times 10^5$ N/m^2.

Even if we take into account the increase in the number density of ions due to the radiolysis of water by TEM electrons[37], which changes the value of ion density from around 3.0×10^{-6} mol/L to 6.5×10^{-5} mol/L, the force of attraction is only $\Pi_{EDL} = 48.1$ N/m^2 at a distance of 2 nm; this is still far smaller than the obtained van der Waals force. Therefore, the force acting between the bubble and the flake is always repulsion. The fact that the van der Waals force becomes repulsion and the electric double layer force becomes attractive is a common phenomenon between asymmetric surfaces[33,34]; thus it is qualitatively correct that a repulsive force acts between flakes and bubbles. We will compare the magnitude of this pressure with the pressure calculated from the deformation of the gas-liquid interface, shown in Figure 3.

$$\Delta E = \gamma_{LG}\{(l_2 - l_1)h\} + (\gamma_{SL} - \gamma_{SG})A \tag{6}$$

$$\Pi = \frac{\Delta E}{x}\frac{1}{l_1 h} \tag{7}$$

Eq. (6) evaluates the change in surface energy due to bubble deformation, and equation (7) gives the pressure required for that deformation. Derivation of eq. (6) is described in the supporting information. Here γ is the surface tension, l_1 and l_2 are the lengths of the gas-liquid interface before and after deformation (which can be measured from Figure 3), h is the thickness of the bubble, x is the distance the flake pushed into the gas-liquid interface, and A is the newly wetted area. Subscripts S, L, and G denote the solid, liquid, and gas phases, respectively. Since we assumed that the bubble is cylindrical, i.e., has a contact angle of 90°, the second term on the right-hand side of eq. (6) can be ignored, according to Young's equation. We estimated the bubble height to be 10 nm. The dimensions and other quantities for the three flakes shown in Figure 3 are listed in the supporting information. Using the surface tension γ_{LG} = 0.07286 N/m^2, the average value of the pressure was 1.17 × 10^6 N/m^2, which is one order of magnitude larger than the one obtained from the DLVO theory. From this comparison, although there are inevitable errors caused by the assumption of the physical properties used in the van der Waals force and electrostatic force calculations, the DLVO theory can qualitatively explain the phenomenon of non-contact pinning when a thin water film is pushed by a growing bubble, as shown in Figure 3. A more rigorous comparison between experimental results and theoretical prediction will be achieved by using a non-polarized liquid such as n-hydrocarbons and/or by quantifying the hydration force[33], but it is beyond the scope of the present paper.

Attractive force-like phenomenon

Furthermore, we observed that two flakes temporarily stopped the gas-liquid interface moving away from them, as shown in Figure 4. The bubble started to grow as soon as the observation started (Figure 4 (b and c)), which indicated that the bubble absorbed the hydrogen and oxygen molecules generated by the radiolysis of water by the electron beam[37]. During the growth of the bubble, the water films between flakes 1 and 2 also maintained their thickness of approximately 2 nm, same as Figure 3. Thirteen seconds after the start of observation (Figure 4(c)), the bubble began to shrink. This shrinkage was caused by electron beam damage to the graphene covering the bubble, and subsequent leakage of the gas into the TEM column[29]. During the shrinkage, the upper right and lower left gas-liquid interfaces pinned by flakes 1 and 2, as depicted by dashed red lines in Figure 4(a), did not move; instead, the shrinkage proceeded from the unpinned areas (Figure 4(c–f)). As a result, the gas-liquid interface pinned by flake 1 became spiky (Figure 4(f)). After 19 seconds from the start of observation, the bubble was no longer stopped by flake 1, and the gas-liquid interface near flake 1 suddenly moved to make a more thermodynamically favorable shape (Figure 4(f-h)).

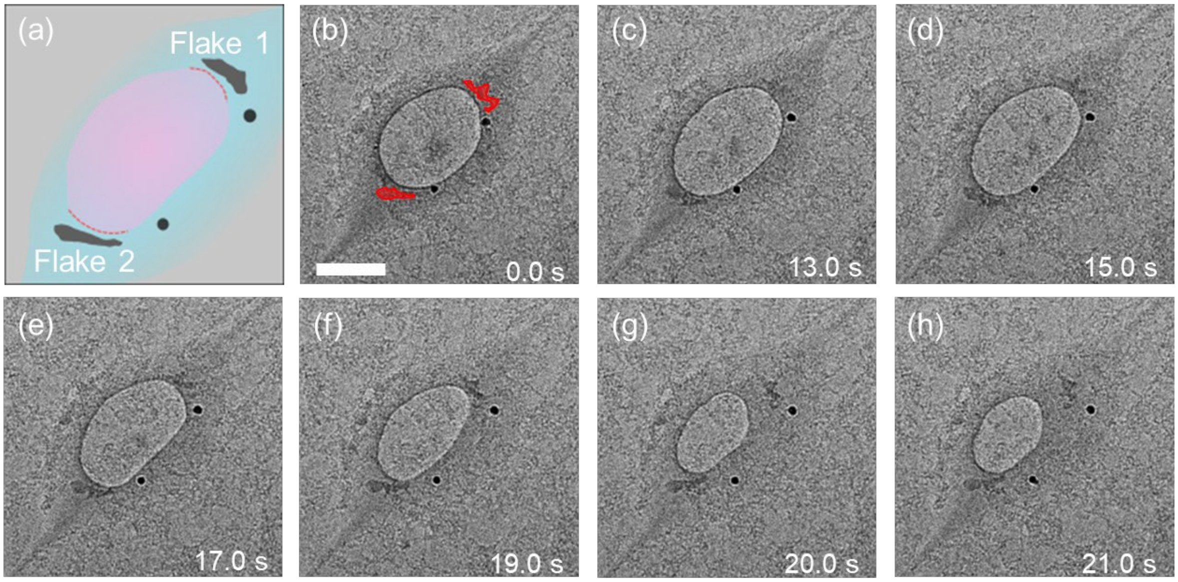

Figure 4 Schematic of a GLC with a bubble temporarily pinned by two flakes (a). Blue part is water and the pink part is a bubble. Snapshots of the bubble (b–h). The pinned part of the three-phase contact line is indicated by the dashed red lines in (a). Two flakes are colored red in (b). The scale bar is 50 nm.

As discussed above, the repulsive force derived from van der Waals force is dominant in the 2 nm-thick water film, so the attractive force that occurred when the bubble began to shrink, shown in Figure 4, cannot be explained by DLVO theory. We believe that this phenomenon can be explained by the unique behavior of water molecules trapped in nanoscale space. It has been reported that water molecules near the solid surface (in this case, the graphene and the flakes) form a tightly ordered structure, or hydration layer, caused by their strong interaction with the solid surface[38]. AFM measurements of graphite, mica, and other substrates in water revealed the hydration layer extends at least 1 nm from the solid surface[39,40]. The size of the liquid film in the height direction in Figure 4 is less than 5 nm, judging from the diameter of the nearby nanoparticle that was sandwiched by the upper and bottom graphene sheets. If we estimate the thickness of the liquid film to be 2 nm, the water molecules inside the liquid film surrounded by solid surfaces on three sides are likely to be regularly aligned for the most part. It can be concluded that the force required to break this ordered molecular structure is the other origin of attractive force-like phenomenon. The force to break the hydration layer was mentioned in a previous study[38]; Fukuma *et al.* reported a comparison of AFM data and MD results, and noted that the hydration layer can be measured with AFM because the force is applied when the probe contacts the hydration layer and pushes it away[41]. Moreover, it is known that the interaction with a solid surface also reduces the mobility of water molecules near the hydration layer. The diffusion coefficient of water, 10^{-9} m^2/s, decreases significantly inside "nanospaces"[42–44]; Lu *et al.* studied Brownian motion of gold nanoparticles and revealed that diffusion coefficient became 10^{-18} m^2/s in 10-20 nm diameter droplets[45]. This means that the local viscosity of water is much higher in the vicinity of the solid, whereas the local mobility of water is much lower than in the bulk. This reduced mobility delays the supply of new water molecules, which would be needed for the liquid film to expand. Therefore, the attractive force-like phenomenon shown in Figure 4 can be qualitatively explained by the fact that energy is required to rearrange the ordered structure of water molecules inside the liquid film, and that the high viscosity near the solid slows down the influx of water molecules from the surrounding liquid. It is important to note that these two factors explaining the attractive force between the bubble and flake are only applicable to the nano-confined situations. Altogether, our results provide an important insight towards nanoscale pinning and is an important step forward to control the fluids in nano-space.

Conclusions

Using liquid phase electron microscopy, we observed the nanoscale bubbles enclosed in a graphene liquid cell to explore the origin of the pinning of the solid-liquid-gas three-phase boundary. The highlight of our study is the observation of two different liquid-gas interface pinning models: contact and non-contact pinning. We confirmed that the sub-nanometer surface contaminations on the graphene surface did not affect the dynamics or shape of the gas-liquid interface of the bubbles as the bubble is sufficiently taller than the surface heterogeneities. We found that nanoparticles with diameters of 2–10 nm can pin the gas-liquid interface via direct contact, however, the contact angle could not be determined due to the inherent difficulty in determining the exact position of the gas-liquid interface. Interestingly, we observed non-contact pinning of the gas-liquid interface near a flake-like material. This observation expands the conventional idea of pinning which considers surface roughness and chemical inhomogeneity to be the origin of pinning. To explain this non-contact pinning, we considered the effect of van der Waals forces and the electric double layer forces between the gas-liquid interface and the flake. We also observed the tendency of flakes to prevent the gas-liquid interface from moving away, which cannot be explained by DLVO theory. We conclude that the attractive force-like phenomenon can be qualitatively explained by taking two factors into account: (1) energy is required to reorient aligned water molecules inside the liquid film, and (2) the high viscosity near the solid surface decreased the inflow of water molecules from the surrounding area. We believe that our study is a major step forward in our understanding of the origin of contact line pinning behavior at nanoscale.

Acknowledgments

This work was partially supported by the Japan Science and Technology Core Research for Evolutional Science and Technology （CREST）（Grant No. JPMJCR18I1), the Japan Society for the Promotion of Science Grants-in-Aid for Scientific Research （KAKENHI）（Grant Numbers. JP20H02089, JP20H02090), Japan, and Grant-in-Aid for JSPS Fellows （Grant Number. 21J21976). TEM observations were performed at the Ultramicroscopy Research Center at Kyushu University. We thank Mr. Tatsuya Ikuta, Mr. Sarthak Nag, and Mr. Ryota Kimura for fruitful discussions and technical support.

Supporting Information

File includes original TEM images, calculation of ion density, and data for flakes; supporting movie shows the attractive force-like phenomenon shown in Figure 4.

References

(1) Shen, F.; Li, Y.; Liu, Z.; Li, X. J. Study of Flow Behaviors of Droplet Merging and Splitting in Microchannels Using Micro-PIV Measurement. *Microfluid. Nanofluidics* **2017**, *21*, 1–25.

(2) Lu, Y.; Sathasivam, S.; Song, J.; Crick, C. R.; Carmalt, C. J.; Parkin, I. P. Robust Self-Cleaning Surfaces That Function When Exposed to Either Air or Oil. *Science* **2015**, *347,* 1132 – 1135.

(3) Daniel, S.; Chaudhury, M. K.; Chen, J. C. Fast Drop Movements Resulting from the Phase Change on a Gradient Surface. *Science* **2001**, *291,* 633 – 636.

(4) Lohse, D.; Zhang, X. Pinning and Gas Oversaturation Imply Stable Single Surface Nanobubbles. *Phys. Rev. E - Stat. Nonlinear, Soft Matter Phys.* **2015**, *91*, 1–5.

(5) Alheshibri, M.; Qian, J.; Jehannin, M.; Craig, V. S. J. A History of Nanobubbles. *Langmuir* **2016**, *32*, 11086–11100.

(6) Brotchie, A.; Zhang, X. H. Response of Interfacial Nanobubbles to Ultrasound

Irradiation. *Soft Matter* **2011**, *7*, 265–269.

(7) Dockar, D.; Borg, M. K.; Reese, J. M. Mechanical Stability of Surface Nanobubbles. *Langmuir* **2019**, *35*, 9325–9333.

(8) Zhang, X.; Lhuissier, H.; Sun, C.; Lohse, D. Surface Nanobubbles Nucleate Microdroplets. *Phys. Rev. Lett.* **2014**, *112*, 1–5.

(9) Liu, Y.; Bernardi, S.; Widmer-Cooper, A. Stability of Pinned Surface Nanobubbles against Expansion: Insights from Theory and Simulation. *J. Chem. Phys.* **2020**, *153*, 024704.

(10) Heim, L. O.; Bonaccurso, E. Measurement of Line Tension on Droplets in the Submicrometer Range. *Langmuir* **2013**, *29*, 14147–14153.

(11) Paxson, A. T.; Varanasi, K. K. Self-Similarity of Contact Line Depinning from Textured Surfaces. *Nat. Commun.* **2013**, *4*, 1-8.

(12) Encarnación Escobar, J. M.; García-González, D.; Dević, I.; Zhang, X.; Lohse, D. Morphology of Evaporating Sessile Microdroplets on Lyophilic Elliptical Patches. *Langmuir* **2019**, *35*, 2099–2105.

(13) Zhang, X.; Chan, D. Y. C.; Wang, D.; Maeda, N. Stability of Interfacial Nanobubbles. *Langmuir* **2013**, *29*, 1017–1023.

(14) Tocci, G.; Joly, L.; Michaelides, A. Friction of Water on Graphene and Hexagonal Boron Nitride from Ab Initio Methods: Very Different Slippage despite Very Similar Interface Structures. *Nano Lett.* **2014**, *14*, 6872–6877.

(15) Yamaguchi, Y.; Kusudo, H.; Surblys, D.; Omori, T.; Kikugawa, G. Interpretation of Young's Equation for a Liquid Droplet on a Flat and Smooth Solid Surface: Mechanical and Thermodynamic Routes with a Simple Lennard-Jones Liquid. *J. Chem. Phys.* **2019**, *150*, 044701.

(16) Teshima, H.; Takata, Y.; Takahashi, K. Adsorbed Gas Layers Limit the Mobility of Micropancakes. *Appl. Phys. Lett.* **2019**, *115*, 071603.

(17) Yen, T. H.; Chen, Y. L.; Lin, C. H. Effects of Gas Adsorption and Surface Conditions on Interfacial Nanobubbles. *Langmuir* **2021**, *37*, 2759–2770.

(18) Umeda, K.; Zivanovic, L.; Kobayashi, K.; Ritala, J.; Kominami, H.; Spijker, P.; Foster, A. S.; Yamada, H. Atomic-Resolution Three-Dimensional Hydration

Structures on a Heterogeneously Charged Surface. *Nat. Commun.* **2017**, *8*, 1–9.

(19) Umeda, K.; Kobayashi, K.; Minato, T.; Yamada, H. Atomic-Level Viscosity Distribution in the Hydration Layer. *Phys. Rev. Lett.* **2019**, *122*, 116001.

(20) Fang, C. K.; Ko, H. C.; Yang, C. W.; Lu, Y. H.; Hwang, I. S. Nucleation Processes of Nanobubbles at a Solid/Water Interface. *Sci. Rep.* **2016**, *6*, 1–10.

(21) Park, J.; Koo, K.; Noh, N.; Chang, J. H.; Cheong, J. Y.; Dae, K. S.; Park, J. S.; Ji, S.; Kim, I. D.; Yuk, J. M. Graphene Liquid Cell Electron Microscopy: Progress, Applications, and Perspectives. *ACS Nano* **2021**, *15*, 288–308.

(22) Takesaki, Y.; Kawahara, K.; Hibino, H.; Okada, S.; Tsuji, M.; Ago, H. Highly Uniform Bilayer Graphene on Epitaxial Cu-Ni(111) Alloy. *Chem. Mater.* **2016**, *28*, 4583–4592.

(23) Bunch, J. S.; Verbridge, S. S.; Alden, J. S.; Van Der Zande, A. M.; Parpia, J. M.; Craighead, H. G.; McEuen, P. L. Impermeable Atomic Membranes from Graphene Sheets. *Nano Lett.* **2008**, *8*, 2458–2462.

(24) Berry, V. Impermeability of Graphene and Its Applications. *Carbon N. Y.* **2013**, *62*, 1–10.

(25) Leenaerts, O.; Partoens, B.; Peeters, F. M. Graphene: A Perfect Nanoballoon. *Appl. Phys. Lett.* **2008**, *93*, 11–13.

(26) Barreiro, A.; Börrnert, F.; Avdoshenko, S. M.; Rellinghaus, B.; Cuniberti, G.; Rümmeli, M. H.; Vandersypen, L. M. K. Understanding the Catalyst-Free Transformation of Amorphous Carbon into Graphene by Current-Induced Annealing. *Sci. Rep.* **2013**, *3*, 1-6.

(27) Algara-Siller, G.; Lehtinen, O.; Turchanin, A.; Kaiser, U. Dry-Cleaning of Graphene. *Appl. Phys. Lett.* **2014**, *104*, 3–6.

(28) Lin, L.; Zhang, J.; Su, H.; Li, J.; Sun, L.; Wang, Z.; Xu, F.; Liu, C.; Lopatin, S.; Zhu, Y.; et al. Towards Super-Clean Graphene. *Nat. Commun.* **2019**, *10*, 1–7.

(29) Hirokawa, S.; Teshima, H.; Solís-Fernández, P.; Ago, H.; Tomo, Y.; Li, Q. Y.; Takahashi, K. Nanoscale Bubble Dynamics Induced by Damage of Graphene Liquid Cells. *ACS Omega* **2020**, *5*, 11180–11185.

(30) Joanny, J. F.; Gennes, P. G. De; Introduction, I. A Model for Contact Angle Hysteresis. *J. Chem. Phys.* **1984**, *81*, 552–562.

(31) Andrews, D. H. The Collected Works of J. Willard Gibbs. Two Volumes. *J. Chem. Educ.* **1929**, *6*, 591.

(32) Naeiji, P.; Woo, T. K.; Alavi, S.; Varaminian, F.; Ohmura, R. Interfacial Properties of Hydrocarbon/Water Systems Predicted by Molecular Dynamic Simulations. *J. Chem. Phys.* **2019**, *150*, 114703.

(33) Israelachvili, J. N. Chapter 13 - Van Der Waals Forces between Particles and Surfaces; Israelachvili, J. N. B. T.-I. and S. F. (Third E., Ed.; Academic Press: San Diego, 2011; pp 253–289.

(34) Israelachvili, J. N. Chapter 14 - Electrostatic Forces between Surfaces in Liquids; Israelachvili, J. N. B. T.-I. and S. F. (Third E., Ed.; Academic Press: San Diego, 2011; pp 291–340.

(35) Meegoda, J. N.; Hewage, S. A.; Batagoda, J. H. Application of the Diffused Double Layer Theory to Nanobubbles. *Langmuir* **2019**, *35*, 12100–12112.

(36) Bepete, G.; Anglaret, E.; Ortolani, L.; Morandi, V.; Huang, K.; Pénicaud, A.; Drummond, C. Surfactant-Free Single-Layer Graphene in Water. *Nat. Chem.* **2017**, *9*, 347–352.

(37) Schneider, N. M.; Norton, M. M.; Mendel, B. J.; Grogan, J. M.; Ross, F. M.; Bau, H. H. Electron-Water Interactions and Implications for Liquid Cell Electron Microscopy. *J. Phys. Chem. C* **2014**, *118*, 22373–22382.

(38) Teshima, H.; Li, Q. Y.; Takata, Y.; Takahashi, K. Gas Molecules Sandwiched in Hydration Layers at Graphite/Water Interfaces. *Phys. Chem. Chem. Phys.* **2020**, *22*, 13629–13636.

(39) Suzuki, K.; Oyabu, N.; Kobayashi, K.; Matsushige, K.; Yamada, H. Atomic-Resolution Imaging of Graphite-Water Interface by Frequency Modulation Atomic Force Microscopy. *Appl. Phys. Express* **2011**, *4*, 125102.

(40) Yang, C. W.; Miyazawa, K.; Fukuma, T.; Miyata, K.; Hwang, I. S. Direct Comparison between Subnanometer Hydration Structures on Hydrophilic and Hydrophobic Surfaces via Three-Dimensional Scanning Force

Microscopy. *Phys. Chem. Chem. Phys.* **2018**, *20*, 23522–23527.

(41) Fukuma, T.; Reischl, B.; Kobayashi, N.; Spijker, P.; Canova, F. F.; Miyazawa, K.; Foster, A. S. Mechanism of Atomic Force Microscopy Imaging of Three-Dimensional Hydration Structures at a Solid-Liquid Interface. *Phys. Rev. B - Condens. Matter Mater. Phys.* **2015**, *92*, 1–7.

(42) Zheng, H.; Claridge, S. A.; Minor, A. M.; Alivisatos, A. P.; Dahmen, U. Nanocrystal Diffusion in a Liquid Thin Film Observed by in Situ Transmission Electron Microscopy. *Nano Lett.* **2009**, *9*, 2460–2465.

(43) Grogan, J. M.; Rotkina, L.; Bau, H. H. In Situ Liquid-Cell Electron Microscopy of Colloid Aggregation and Growth Dynamics. *Phys. Rev. E - Stat. Nonlinear, Soft Matter Phys.* **2011**, *83*, 1–5.

(44) Verch, A.; Pfaff, M.; De Jonge, N. Exceptionally Slow Movement of Gold Nanoparticles at a Solid/Liquid Interface Investigated by Scanning Transmission Electron Microscopy. *Langmuir* **2015**,*31*, 6956–6964.

(45) Lu, J.; Aabdin, Z.; Loh, N. D.; Bhattacharya, D.; Mirsaidov, U. Nanoparticle

Dynamics in a Nanodroplet. *Nano Lett.* **2014**, *14*, 2111–2115.

Graphic Abstract